

Two stream instability - Numerical Physics project

Qien Jing, Han Zhao

December 2025

1 Introduction

The two stream instability is a fundamental collective phenomenon in plasma physics and serves as a canonical model for studying the self-consistent interaction between charged particles and electrostatic fields. It captures key kinetic processes such as wave particle interaction and nonlinear trapping. Because these mechanisms arise from the detailed structure of the velocity distribution function $f(v)$, rather than fluid moments like the average velocity, they lie beyond the capability of magnetohydrodynamic (MHD) models, which assume a single bulk velocity and an approximately Maxwellian distribution at all times. When forward-accelerated electrons encounter decelerated ones, two distinct velocity streams may coexist, making fluid descriptions inadequate.

A fully kinetic treatment is therefore required. Solving the Vlasov equation is ideal but computationally demanding, whereas the Particle-in-Cell (PIC) method provides a practical alternative: it evolves particle trajectories and electromagnetic fields self-consistently at considerably lower cost. Widely used across plasma physics, astrophysics, and accelerator science, PIC combines a Lagrangian representation of charged particles with an Eulerian field solver. Its core cycle consists of charge deposition, field solving, field gathering, and particle pushing.

In this work, we focus on a simplified **1D3V electrostatic PIC system**, where the spatial domain is one-dimensional with periodic boundaries while particles retain three velocity components. Only the longitudinal electric field E_x is solved from Poisson's equation; transverse fields and magnetic fields are included as placeholders for future extension to a full electromagnetic PIC model.

Electrons are initialized in a two beam configuration with opposite beam velocities, exciting the classical two stream instability. The objective of this report is to describe the code implementation, validate its linear growth rates against theory, and analyze nonlinear saturation and the resulting phase space structures. To support future extensions, we developed a fully functional and modular 1D3V electrostatic PIC code.

2 Two stream Instability: Fluid Theory

In order to interpret the results obtained from the PIC simulation, it is useful to derive the theoretical dispersion relation of the cold two stream instability. Under the cold-plasma approximation, the electron distribution function collapses into a Dirac delta function, which implies that the Vlasov equation becomes equivalent to its lower-order moment equations (the fluid equations). In this regime, the dispersion relation of the two stream instability can be derived directly from the fluid formulation.

We consider a one-dimensional electrostatic system consisting of two cold electron beams propagating in opposite directions with beam velocities $+v_0$ and $-v_0$. The ions form a fixed neutralizing background ($n_{i1} = 0$). Each electron beam has density $n_0/2$, so that the total electron plasma frequency is

$$\omega_p^2 = \frac{n_0 e^2}{\epsilon_0 m}.$$

2.1 Linearized fluid equations

For each electron beam ($j = 1, 2$), the continuity and momentum equations are

$$\frac{\partial n_j}{\partial t} + \nabla \cdot (n_j v_j) = 0, \quad (1)$$

$$m \frac{\partial v_j}{\partial t} = -eE. \quad (2)$$

We linearize around the equilibrium

$$n_j = n_{0j} + n_{1j}, \quad v_j = v_{0j} + v_{1j},$$

with

$$n_{01} = n_{02} = \frac{n_0}{2}, \quad v_{01} = +v_0, \quad v_{02} = -v_0.$$

Assuming perturbations of the form

$$E_1 = E e^{i(kx - \omega t)},$$

the linearized equations become

$$-i(\omega - kv_{0j}) n_{1j} + ik n_{0j} v_{1j} = 0, \quad (3)$$

$$-i(\omega - kv_{0j}) m v_{1j} = -eE. \quad (4)$$

Solving for v_{1j} and n_{1j} yields

$$v_{1j} = \frac{eE}{m(\omega - kv_{0j})}, \quad (5)$$

$$n_{1j} = \frac{ekn_{0j}}{m} \frac{E}{(\omega - kv_{0j})^2}. \quad (6)$$

The Poisson equation in Fourier space is

$$ikE = \frac{\rho_1}{\epsilon_0} = -\frac{e}{\epsilon_0}(n_{11} + n_{12}),$$

where ions do not contribute ($n_{i1} = 0$). Substituting the density perturbations gives

$$1 = \sum_{j=1}^2 \frac{n_{0j} e^2}{\epsilon_0 m} \frac{1}{(\omega - kv_{0j})^2} = \sum_{j=1}^2 \frac{\omega_{pj}^2}{(\omega - kv_{0j})^2},$$

with $\omega_{pj}^2 = n_{0j} e^2 / (\epsilon_0 m)$.

For the symmetric two-beam system,

$$\omega_{p1}^2 = \omega_{p2}^2 = \omega_{p,beam}^2 = \frac{\omega_p^2}{2}, \quad v_{01} = +v_0, \quad v_{02} = -v_0,$$

so the dispersion relation becomes

$$1 = \omega_{p,beam}^2 \left[\frac{1}{(\omega - kv_0)^2} + \frac{1}{(\omega + kv_0)^2} \right]. \quad (7)$$

2.2 Most unstable mode and growth rate

To determine the most unstable mode of the symmetric cold two stream instability, we start from the cold-fluid dispersion relation for two counter-propagating beams of velocity $\pm v_0$,

$$1 - \frac{\omega_p^2}{(\omega - kv_0)^2} - \frac{\omega_p^2}{(\omega + kv_0)^2} = 0. \quad (8)$$

Expanding the denominators and collecting terms gives a quartic equation in ω ,

$$\omega^4 - 2\omega^2(k^2v_0^2 + \omega_p^2) + k^4v_0^4 - 2k^2v_0^2\omega_p^2 = 0. \quad (9)$$

Let $X = \omega^2$, so that the dispersion relation becomes a quadratic equation,

$$X^2 - 2(k^2v_0^2 + \omega_p^2)X + k^4v_0^4 - 2k^2v_0^2\omega_p^2 = 0. \quad (10)$$

The unstable branch is the one with $X = \omega^2 < 0$. Solving the quadratic gives

$$\omega^2 = k^2v_0^2 + \omega_p^2 - \omega_p\sqrt{4k^2v_0^2 + \omega_p^2}. \quad (11)$$

Inside the unstable region $\omega = i\gamma$, therefore

$$\gamma^2 = \omega_p\sqrt{4k^2v_0^2 + \omega_p^2} - (k^2v_0^2 + \omega_p^2). \quad (12)$$

Define a dimensionless parameter $a \equiv kv_0/\omega_p$, which yields the normalized growth rate

$$\frac{\gamma^2}{\omega_p^2} = \sqrt{4a^2 + 1} - (a^2 + 1) \equiv f(a). \quad (13)$$

The most unstable mode satisfies $\frac{df}{da} = 0$, thus the wavenumber of the most unstable mode is

$$a = \frac{\sqrt{3}}{2} \Rightarrow k_{\max} = \frac{\sqrt{3}}{2}\omega_p/v_0 \approx 0.866\omega_p. \quad (14)$$

Substituting $a^2 = 3/4$ back into $f(a)$ gives

$$\gamma_{\max} = \frac{\omega_p}{2}. \quad (15)$$

These theoretical analysis fully consistent with numerical calculation shown in Fig. 1, and also provides a useful benchmark for comparison with the PIC simulation results.

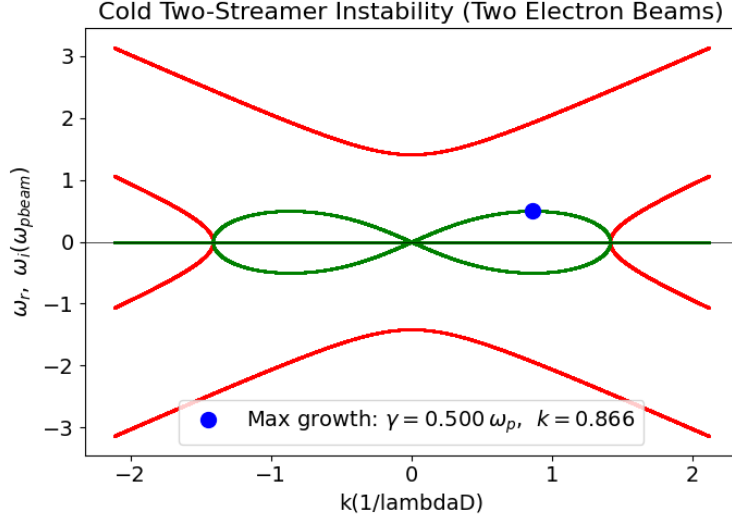


Figure 1: Theoretical calculation of the dispersion relation for $\hat{v}_0 = 1$

3 Numerical Method

3.1 Normalization

PIC simulations usually implement the normalized (or dimensionless) formulation. The motivation for the normalization is that it reduces numerical difficulties caused by the large physical scales in SI units, while simultaneously making the algorithm independent of any specific choice of physical units and therefore easily adapted to a wide range of plasma conditions. The normalization we used is in below:

We use the reference thermal speed corresponding to $T = 1 \text{ eV}$,

$$v_{\text{th,ref}} = \sqrt{\frac{T_e}{m_e}} \quad (16)$$

Note that the thermal speed corresponding to $T = 1 \text{ eV}$ is used merely as a reference normalization unit. Both the beam velocity v_0 and the thermal speed v_{th} in the simulations are expressed in units of this reference speed. Unless otherwise stated, The system remains in the cold plasma limit because we keep the ratio $v_{th}/v_0 = 0.1$ in all simulations, while the framework retain the flexibility to explore finite temperature cases when needed.

The electron plasma frequency, where n_0 is the density of each streamer,

$$\omega_p = \sqrt{\frac{n_0 e^2}{\epsilon_0 m_e}} \quad (17)$$

which defines the Debye length $\lambda_D = v_{\text{th,ref}}/\omega_p$.

The dimensionless quantities used in the simulation are

$$\hat{x} = \frac{x_{\text{SI}}}{\lambda_D}, \quad \hat{t} = \omega_p t_{\text{SI}}, \quad \hat{v} = \frac{v_{\text{SI}}}{v_{\text{th,ref}}}, \quad \hat{E} = \frac{e E_{\text{SI}}}{m_e v_{\text{th,ref}} \omega_p}, \quad \hat{\rho} = \frac{\rho_{\text{SI}}}{n_0 e}, \quad \hat{W} = \frac{W_{\text{SI}}}{n_0 m_e v_{\text{th,ref}}^2} \quad (18)$$

where \hat{x} , \hat{t} , \hat{v} , \hat{E} , $\hat{\rho}$, \hat{W} are the dimensionless formula of particle position, simulation time, particle velocity, electric field, kinetic or electric energy, respectively.

Under this normalization, fundamental physics constants and quantities are measured in units of ω_p^{-1} , λ_D , and $v_{\text{th,ref}}$, so that the dimensionless equations take the form where

$$e = m_e = \epsilon_0 = n_0 = 1, \quad \hat{\omega}_p = \hat{\lambda}_D = \hat{v}_{\text{th,ref}} = 1$$

where hats denote dimensionless quantities.

3.2 PIC algorithm validation

Before studying the physical two stream instability, we first checked that the basic numerical components of the PIC loop are correctly implemented. All test scripts used for validating individual modules are organized in the dedicated TEST directory. The PIC cycle used in this work consists of four main modules:

1. **Charge deposition:** map particle charges onto the grid using a Cloud-In-Cell (CIC) shape function;
2. **Poisson solver:** solve the electrostatic Poisson equation on the grid to obtain the potential and electric field;
3. **Field gather:** interpolate the grid-based electric field back to particle positions using the same CIC weights;
4. **Particle push:** advance particle positions and velocities using the standard Boris pusher.

Each module was tested individually with simple configurations in which the expected solution is known, allowing us to verify correctness before running the full PIC simulation.

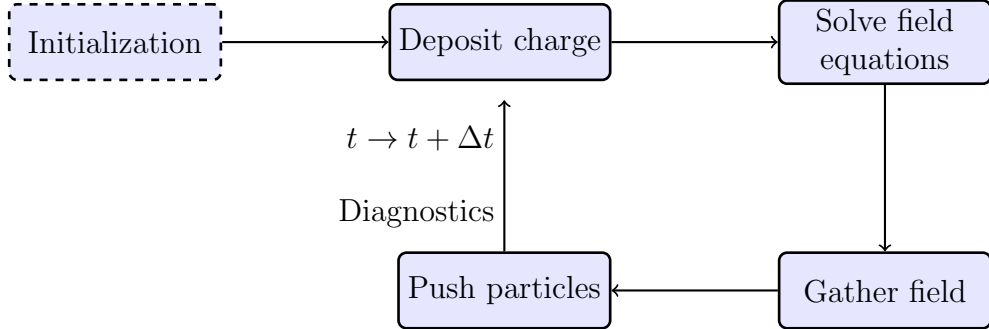


Figure 2: Main loop of a Particle in Cell (PIC) simulation.

3.2.1 Deposit charge

To check the implementation of the charge deposition routine, we designed a simple test with three macro-particles on a 1D grid of length $L_x = 1$ and $N_x = 16$ cells. The particle positions and charges are

$$x_p = (0.10, 0.37, 0.92), \quad q_p = (-1.0, 0.5, -0.2),$$

so that one particle lies close to the left boundary, one in the interior of the domain, and one near the right boundary in order to exercise the periodic wrapping. The particles are deposited onto the grid using the CIC scheme, producing a discrete charge density ρ_i .

As a consistency check, we compare the total charge carried by the particles,

$$Q_{\text{part}} = \sum_p q_p,$$

with the total charge obtained from the grid density,

$$Q_{\text{grid}} = \sum_i \rho_i \Delta x,$$

where $\Delta x = L_x/N_x$. In the code, both quantities are printed as Sum of particle charges and Total deposited charge, and their difference is found to be almost the same. This confirms that the deposition algorithm conserves the total charge exactly and behaves as expected for particles located near the periodic boundaries.

3.2.2 Poisson solver

To verify the correctness of the implemented Poisson solver, we tested it against several analytical benchmark cases under periodic boundary conditions. The solver is designed to compute the electrostatic field from the charge density by solving

$$\frac{d^2\phi}{dx^2} = -\rho(x), \quad E(x) = -\frac{d\phi}{dx}.$$

Test cases:

Case 1: $\rho(x) = 0$. The numerical result gives $E \approx 0$ up to round-off level ($\max |E| < 10^{-15}$), confirming the solver preserves the trivial solution.

Case 2: $\rho(x) = \cos(kx)$. The analytical solution is

$$\phi_{\text{ana}}(x) = \frac{\cos(kx)}{k^2}, \quad E_{\text{ana}}(x) = \frac{1}{k} \sin(kx).$$

Numerical results show L_2 error below 10^{-6} for $k = 1, 3$, indicating excellent agreement with theory.

Case 3: high-wavenumber mode ($k = 10$). The solver remains accurate with similarly small L_2 error, demonstrating robustness for short-wavelength components.

Case 4: random $\rho(x)$. The field computed by our solver matches the FFT-reconstructed analytical reference with very small L_2 discrepancy.

Across all tests, the numerical solutions overlap with the analytical results almost perfectly, and the measured L_2 errors are on the order of 10^{-6} to 10^{-10} . This confirms that our Poisson solver is accurate and consistent with theoretical predictions, and is therefore reliable for subsequent PIC simulations.

3.2.3 Gather field

The field gather routine interpolates grid-based quantities back to the particle positions. We again use a CIC scheme, consistent with the charge deposition step. For a particle at position x_p , we locate the indices of the two nearest grid points and compute the fractional coordinate inside the cell. The electric field at the particle is then obtained as a linear combination of the surrounding grid values.

In continuous notation, the field at a particle can be written as

$$F_p = \sum_i F_i S(x_i - x_p),$$

where F_i is the grid field, x_i is the position of grid point i , and S is the same linear shape function used for deposition. In the code this reduces to

$$F_p = w_L F_{i_L} + w_R F_{i_R},$$

with $w_L = 1 - \xi$ and $w_R = \xi$ the CIC weights determined by the particle position inside the cell. Using the same shape function for both deposition and gathering ensures that the PIC scheme is self-consistent.

3.2.4 Push particle

Boris algorithm

Particle motion is evaluated using the standard Boris algorithm in a leapfrog time discretization.

The Boris integrator exhibits excellent long-term stability when advancing charged particle trajectories. Owing to its leapfrog structure, the method introduces extremely small numerical energy drift even over millions of time steps. This makes the Boris scheme particularly well suited for PIC simulations in which particles must be evolved for long physical durations without artificial damping or secular energy growth.

A key geometric property of the Boris scheme is that it preserves the phase space volume of the particle trajectories,

$$\det\left(\frac{\partial z^{n+1}}{\partial z^n}\right) = 1, \quad z = (\mathbf{x}, \mathbf{v}),$$

ensuring that the algorithm does not introduce artificial compression or expansion of particle orbits. This volume-preserving (near-symplectic) nature prevents unphysical dissipation or numerical heating, and is crucial for accurately capturing Hamiltonian dynamics such as charged-particle motion in electromagnetic fields.

At each time step the code assumes that the particle positions x^n and the velocities $v^{n+1/2}$ are known. The pusher first applies a half electric kick to obtain an intermediate velocity,

$$\mathbf{u} = \mathbf{v}^{n+1/2} + \frac{q}{m} \mathbf{E}^n \frac{\Delta t}{2},$$

then rotates \mathbf{u} around the magnetic field using the Boris rotation, and finally applies a second half electric kick to obtain $\mathbf{v}^{n+3/2}$. The new position is updated with the centered velocity,

$$x^{n+1} = x^n + v_x^{n+1/2} \Delta t,$$

and periodic boundary conditions are enforced by wrapping the position into the interval $[0, L_x]$.

In summary, by isolating and exactly resolving the magnetic field induced rotation, the Boris algorithm preserves kinetic energy and prevents numerical drift, giving it both higher accuracy and greater efficiency than widely used integrators such as forth order Runge-Kutta (RK4).

Validation of push particle

To verify the implementation of the Boris pusher in our 1D3V code, we consider a spatially uniform but time-oscillating electric field and no magnetic field,

$$E_x(t) = E_0 \sin(\omega t), \quad B = 0,$$

with the normalized charge-to-mass ratio $q/m = -1$. The equation of motion then reads

$$\frac{dv_x}{dt} = \frac{q}{m} E_x(t) = -E_0 \sin(\omega t).$$

Integrating from $t = 0$ with initial velocity $v_x(0) = v_0$ gives

$$v_x(t) = v_0 + \frac{E_0}{\omega} (\cos(\omega t) - 1),$$

and a second integration for the position (with $x(0) = x_0$) yields

$$x(t) = x_0 + \left(v_0 - \frac{E_0}{\omega} \right) t + \frac{E_0}{\omega^2} \sin(\omega t).$$

In the code, we evolve a single particle under this electric field using the Boris pusher and record the numerical velocity $v_{\text{num}}(t_n)$ and position $x_{\text{num}}(t_n)$ at each time step. These are compared with the analytical expressions $v_{\text{ana}}(t_n)$ and $x_{\text{ana}}(t_n)$ above. As shown in Fig.1, the numerical and analytical curves for both $v_x(t)$ and $x(t)$ are almost indistinguishable; the Boris pusher accurately reproduces the exact solution for this time-dependent electric field.

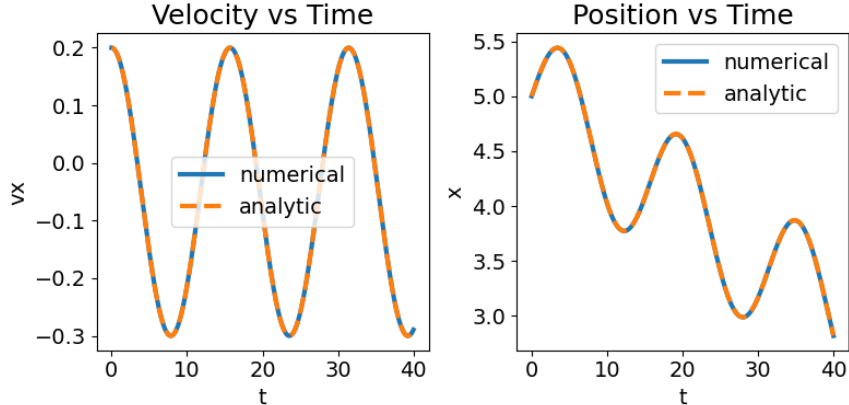


Figure 3: Numerical validation of the Boris pusher under an oscillating electric field

3.3 Simulation setup

To ensure that the results obtained from the PIC simulation are physically reliable a systematic convergence study is required. In this work, we examine the sensitivity of the simulation outputs to variations in the key numerical parameters. When one parameter is varied, the remaining parameters are consistent with those in Table. 1.

Parameter	Value	Note
L_x	$30 \lambda_D$	domain length
N_x	64	grid point
N_p	5×10^5	total particles
dt	0.02	time step
v_0	1.0	beam drift speed
v_{th}	0.1	electron thermal speed
n_0	$1 \times 10^{15} \text{ m}^{-3}$	beam density per stream

Table 1: Simulation parameters used in the PIC runs.

3.3.1 Spatial

The periodic condition of fourier expansion gives $e^{ikL_x} = 1$, which means $k_m = 2\pi m/L_x$ ($m = 1, 2, \dots, N_x/2$). From sec.2, one knows the wave number corresponding to the maximum grow rate: $k_{max} \approx 0.86 \lambda_D^{-1}$ ($\hat{v}_0 = 1$).

Therefore, we choose $L = 30$, which means the mode with $m = 4$ nearly exactly matches the dominant unstable wavenumber. Also, there would be 4 phase space hole, i.e., BGK structure.

To assess spatial convergence, we vary the number of grid points $N_x = 16, 64, 128$, while holding all physical parameters constant, and examine the resulting changes in the growth rate and field structures. We have summarized the results under different spatial resolutions N_x in a table, together with the corresponding phase space distributions shown below. These figures illustrate how the system evolves as N_x increases.

N_x	Measured γ	Convergence behaviour
16	0.344	under-resolved
64	0.4683	near convergence
128	0.4698	converged

Table 2: Measured growth rate γ for different spatial resolutions N_x .

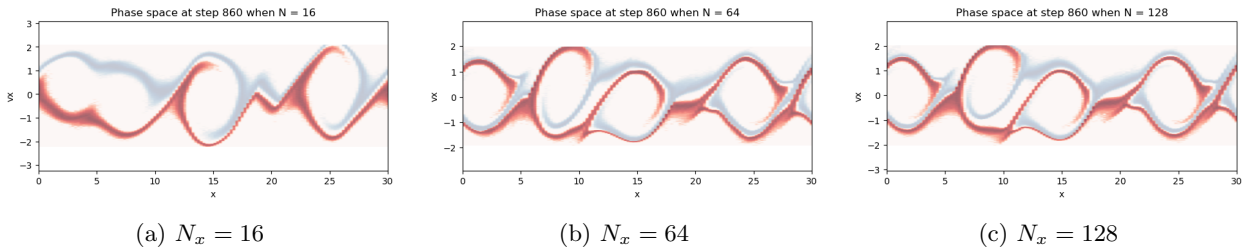


Figure 4: phase space plots under different grid resolutions N_x .

As the grid resolution increases, the computational cost grows rapidly. Therefore, we adopt $N_x = 64$ as it provides sufficient accuracy while maintaining reasonable efficiency.

3.3.2 Particle number

Following the analysis in the previous section, we fix the grid resolution at $N_x = 64$ and investigate the effect of the particle number N_p on the measured growth rate. The corresponding results are listed in Table. 3. In this and the following parts, we continue to fix all the simulation parameters except the one under investigation.

Growth rate vs particle number N_p		
N_p	Measured γ	Convergence behaviour
1×10^5	0.4321	under-sampled
5×10^5	0.4683	near convergence
1×10^6	0.4739	converged

Table 3: Simulation parameters and measured growth rate for different particle numbers

3.3.3 Time

Similarly, we now fix the spatial resolution and particle number at $N_x = 64$ and $N_p = 5 \times 10^5$, and vary the time step dt from 0.01 and 0.02 up to 0.1 to study its influence on the growth rate. From the table, the variation of the growth rate can be clearly observed.

Growth rate vs time step dt		
dt	Measured γ	Comment
0.01	0.4785	converged
0.02	0.4683	converged
0.10	0.4770	nearly converged but not smooth

Table 4: Simulation parameters and growth rate under different time steps

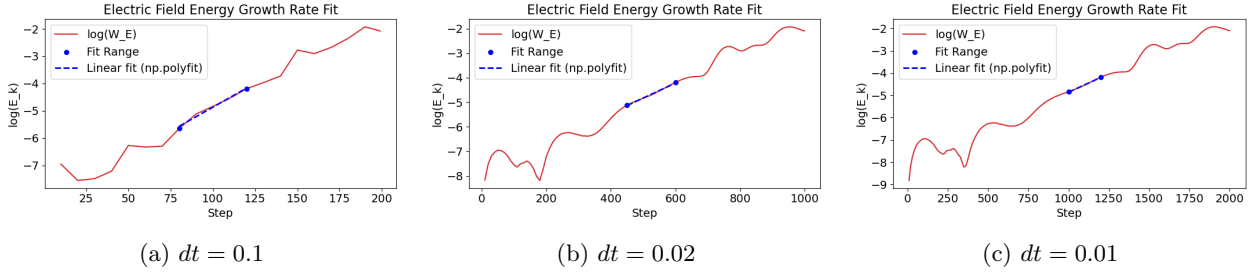


Figure 5: Electric field energy growth rate fitting under different time steps dt when $m = 4$.

Although the table indicates that $\gamma \approx 0.49$ when $dt = 0.1$, the growth curve shows strong numerical noise in the later stage, which can be seen from Table. 4, suggesting that the measurement may not be reliable. Therefore, we choose $dt = 0.02$ as a more accurate and stable setting.

3.4 Full validation of the simulation

In the following, we validate the simulation by examining its correctness from both qualitative and quantitative perspectives.

3.4.1 Qualitative

Based on the convergence analysis above, we adopt the grid resolution, particle number, and time step of $N_x = 64$, $N_p = 5 \times 10^5$, and $\Delta t = 0.02$ for all subsequent simulations, with other parameters specified in Table. 1.

As shown in Fig. 4b, distinct phase space holes, which also known as BGK structures, as discussed in Sec. 3.3.1. For $\hat{v}_0 = 1$, the dispersion relation predicts a dominant mode at $m = 4$, which corresponds to the formation of four BGK structures. This matches the pattern observed in Fig. 4b exactly, confirming that the simulation produces the correct qualitative behavior.

3.4.2 Quantitative

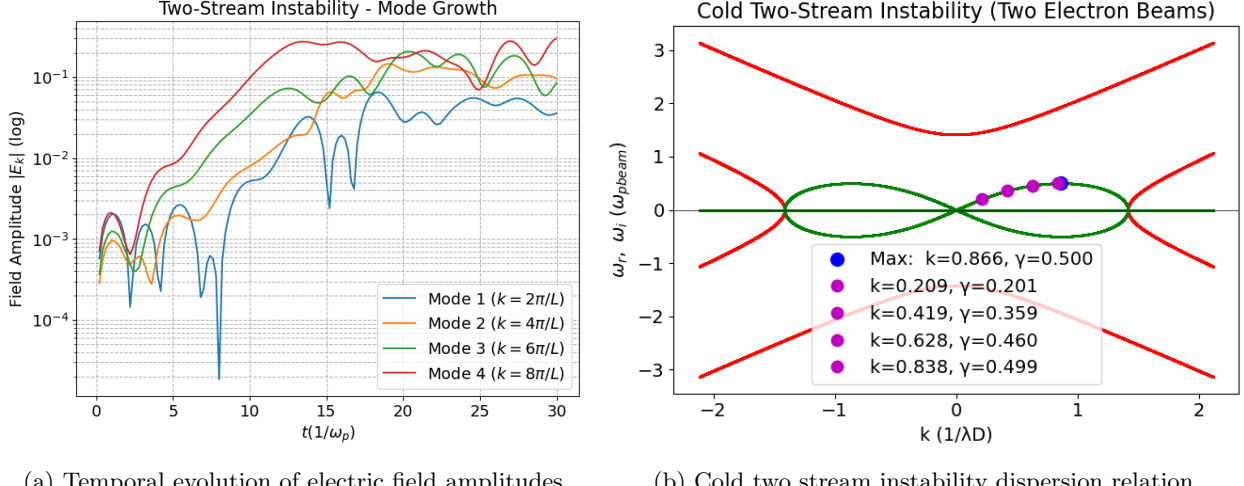
The quantitative correctness of the simulation can be assessed by comparing the growth rate of the dominant mode with the theoretical prediction.

m	Measured γ	Theoretical γ
4	4.68×10^{-1}	5.00×10^{-1}
3	4.32×10^{-1}	4.60×10^{-1}
2	3.30×10^{-1}	3.50×10^{-1}

Table 5: Comparison of measured and theoretical growth rates γ for different mode numbers m .

The Fig. 6a shows that all Fourier modes grow exponentially during the linear stage, with higher-order modes exhibiting faster growth. Mode 4 ($m = 4$) is the fastest-growing mode in our domain and becomes dominant before saturation.

The Fig. 6b presents the analytical cold-beam dispersion relation. The theoretical growth rates for the corresponding wavenumbers ($m = 4, 3, 2$)¹ matches very well with those measured from the PIC simulation. This agreement confirms that our PIC code successfully reproduces the linear instability physics.



(a) Temporal evolution of electric field amplitudes

(b) Cold two stream instability dispersion relation

Figure 6: Mode growth in simulation (left) and corresponding theoretical dispersion relation (right).

¹The blue curve corresponding to $m = 1$ represents a very weak mode whose linear growth stage is not observable. Therefore, it is omitted from the presented results.

4 Results analysis

In the following, we vary the thermal velocity to transition from the cold plasma limit to a finite temperature plasma, allowing us to elucidate the key physical mechanisms of the two stream instability, including the origin of the instability and its saturation process. We further vary the beam velocity to illustrate how different beam speeds modify the mode structure. These results demonstrate the capability of our PIC simulations to capture and analyze the underlying physics.

4.1 From cold plasma to finite temperature plasma——See how the wave particle resonance works

In this part, we computed the growth rate γ from the electric field energy evolution for each case, and plotted γ as a function of v_{th}/v_0 . The curve exhibits a clear decreasing trend: the instability is strongest at low thermal velocity and is gradually suppressed as v_{th} increases, eventually approaching $\gamma \approx 0$ for sufficiently warm beams.

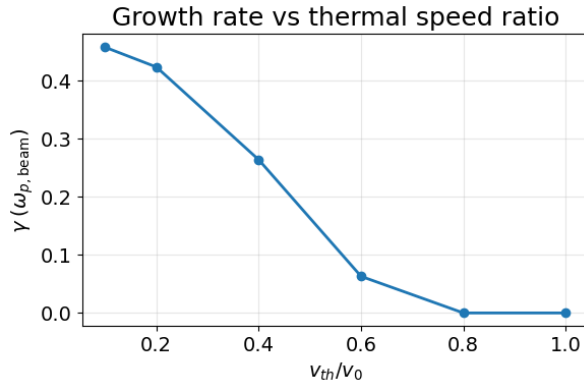


Figure 7: Growth rate γ as a function of the thermal speed ratio v_{th}/v_0 .

As shown in Fig. 8, we analysed the system behaviour for different values of v_{th} . The BGK structure in phase space clearly changes as the thermal velocity increases, indicating stronger phase space mixing and a reduction of coherent trapping structures.

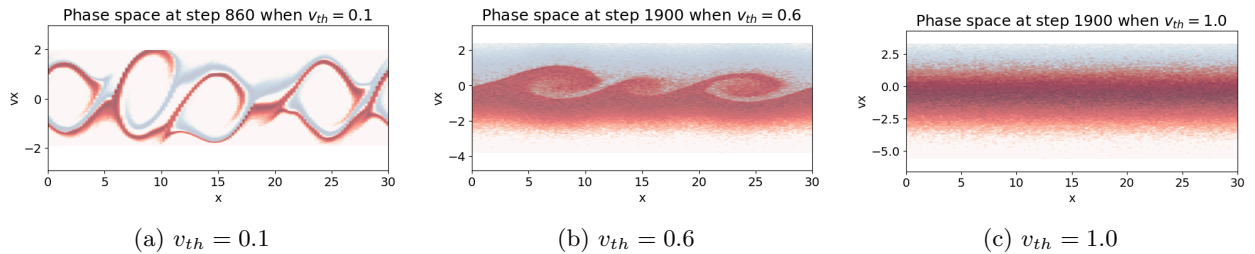


Figure 8: phase space distributions for different thermal velocities v_{th} .

This phenomenon originates from the physical mechanism of the two stream instability, which can be viewed as an extreme case of Landau wave particle resonance. An electrostatic wave exchanges energy with particles whose velocities are close to its phase velocity. When $df/dv < 0$, more particles move slower than the wave and absorb energy from it, leading to damping. In contrast, if $df/dv > 0$, particles transfer their kinetic energy to the wave, causing exponential growth.

For the two stream system, the velocity distribution contains a region with $df/dv > 0$ (the interval between the two beams), as shown in Fig. 10a. In this regime, resonant particles transfer kinetic energy to the field, leading to an exponential growth of the mode during the linear stage. As the system evolves, the wave amplitude increases and eventually becomes strong enough to trap resonant electrons inside its electrostatic potential wells as shown in the center of Fig. 9b Where we used $-\phi$ to represent the electrostatic potential energy of an electron.. These trapped particles execute closed orbits in phase space, giving rise to the characteristic BGK type phase space holes. Through this trapping process, the distribution function is progressively reshaped around the phase velocity, the positive slope region $df/dv > 0$ is flattened as shown in the bottom of Fig. 9b, and the instability ultimately saturates once this region is effectively removed.

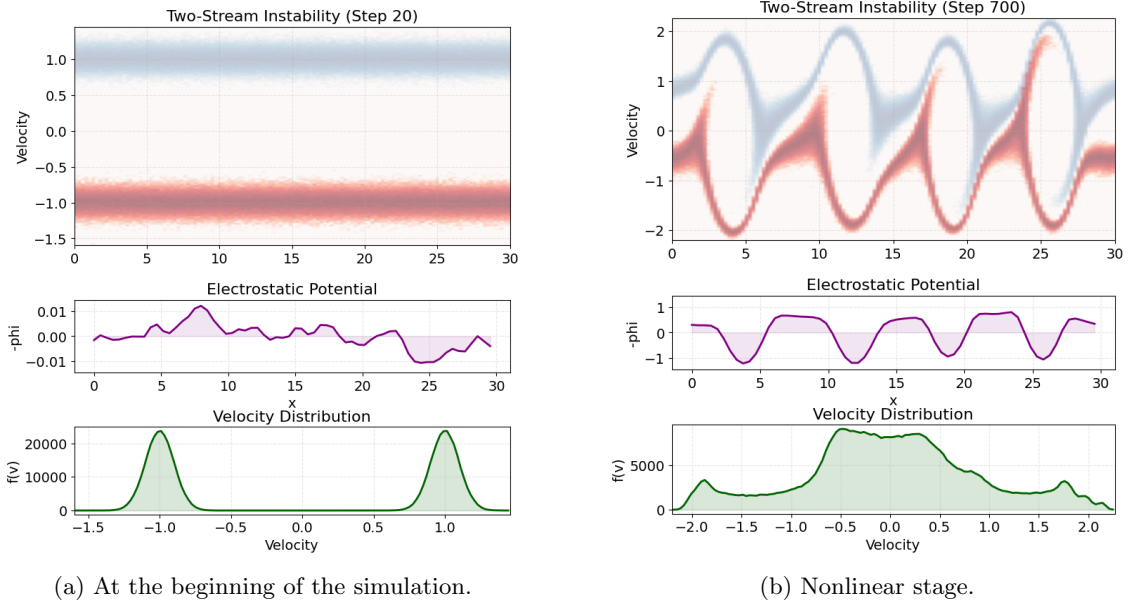


Figure 9: Comparison between the beginning of the simulation and the nonlinear stage of the phase space distribution, electrostatic potential energy and velocity distribution, respectively

When the temperature increases, the two peaks of the distribution broaden and progressively fill the central region. This reduces the magnitude and extent of the $df/dv > 0$ interval, weakening the instability. At sufficiently large temperature, the valley disappears entirely and the distribution becomes single-humped, at which point the instability is suppressed. This result highlights an important advantage of PIC simulations over analytical theory, namely their ability to account for more general and realistic physical conditions.

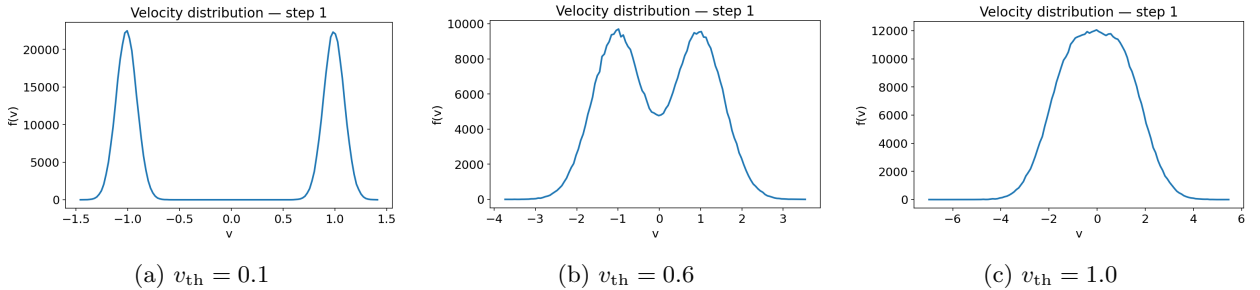


Figure 10: Velocity distribution functions $f(v)$ for different thermal velocities v_{th} in a two stream plasma. Increasing v_{th} broadens each Maxwellian beam and reduces the depth of the central gap between the two streams.

4.2 Different v_0 scan

We also compared the growth rates for different beam velocities v_0 , as shown in Table 6. The variation of the growth rate with respect to v_0 is relatively small, as expected.

v_0	Measured γ	Theoretical γ	Dominant mode
1	4.68×10^{-1}	5.00×10^{-1}	$m = 4$
2	4.75×10^{-1}	5.00×10^{-1}	$m = 2$
3	4.52×10^{-1}	4.60×10^{-1}	$m = 1$

Table 6: Measured and theoretical growth rate γ comparison for different beam speeds v_0 .

From the phase space plots, we also observe that different values of v_0 lead to distinct BGK structures. Although the growth rates remain similar, the qualitative shape of the phase space vortices changes with v_0 . These phase space results are consistent with our prediction in Section 3.3.1, where the number and shape of the BGK structures were shown to depend on the beam velocity v_0 . The simulations clearly reproduce the expected variation in the number of trapped-particle islands, confirming the theoretical analysis.

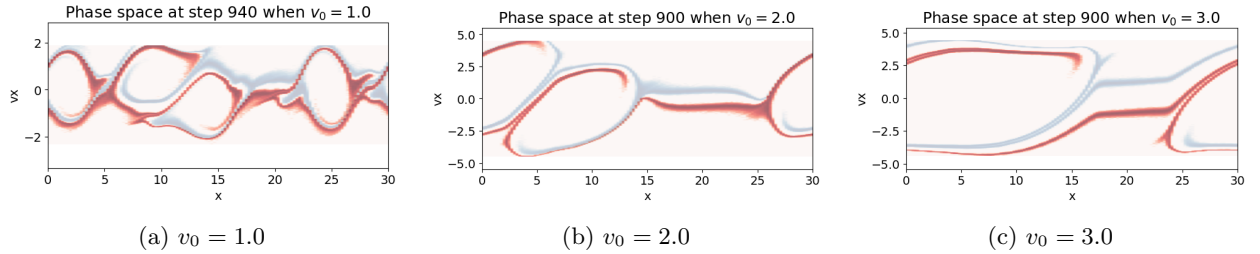


Figure 11: phase space distributions for different beam velocities v_0 .

5 Discuss and Conclusion

In this work, we developed a modular 1D3V electrostatic PIC code capable of simulating the classical two stream instability. By comparing the numerical results with theoretical predictions, we validated both the accuracy of each individual module and the correctness of the integrated system. These tests confirm that the implementation reliably captures the linear growth, nonlinear saturation, and phase space structures associated with the instability.

Furthermore, our simulations allowed us to examine how the system evolves from an initially cold configuration to a thermally broadened state, thereby revealing the key physical mechanisms underlying the two stream instability. We also investigated how different beam velocities influence the resulting unstable modes and phase space dynamics. These results demonstrate the advantages of PIC simulations over purely theoretical analyses.

Because the code is highly modular and includes several reserved interfaces for future extensions, it can be readily expanded to support higher-dimensional geometries and a broader range of physical conditions. This modularity ensures that the current implementation serves not only as a functional solver for the two stream instability but also as a flexible foundation for future PIC development.